

## Article

# NO<sub>x</sub> Storage and Reduction (NSR) Performance of Sr-Doped LaCoO<sub>3</sub> Perovskite Prepared by Glycine-Assisted Solution Combustion

Xinru Luan<sup>1</sup>, Xudong Wang<sup>2</sup>, Tianfei Zhang<sup>3</sup>, Liangran Gan<sup>1</sup>, Jianxun Liu<sup>1</sup>, Yujia Zhai<sup>1</sup>, Wei Liu<sup>1</sup>, Liguo Wang<sup>1</sup> and Zhongpeng Wang<sup>1,\*</sup> 

<sup>1</sup> School of Water Conservancy and Environment, University of Jinan, Jinan 250022, China; 18660155871@163.com (X.L.); 17852863260@163.com (L.G.); ljxx1111@163.com (J.L.); 13853184890@163.com (Y.Z.); stu\_liuw@ujn.edu.cn (W.L.); chm\_wanglg@ujn.edu.cn (L.W.)

<sup>2</sup> Zaozhuang Ecological Environment Monitoring Center of Shandong Province, Zaozhuang 277800, China; bruce004@163.com

<sup>3</sup> School of Materials Science and Engineering, University of Jinan, Jinan 250022, China; 17653136287@163.com

\* Correspondence: chm\_wangzp@ujn.edu.cn; Tel./Fax: +86-531-82769235

**Abstract:** Here, we successfully synthesized Sr-doped perovskite-type oxides of La<sub>1-x</sub>Sr<sub>x</sub>Co<sub>1-λ</sub>O<sub>3-δ</sub>, “LSX” (x = 0, 0.1, 0.3, 0.5, 0.7), using the glycine-assisted solution combustion method. The effect of strontium doping on the catalyst structure, NO to NO<sub>2</sub> conversion, NO<sub>x</sub> adsorption and storage, and NO<sub>x</sub> reduction performance were investigated. The physicochemical properties of the catalysts were studied by XRD, SEM-EDS, N<sub>2</sub> adsorption–desorption, FTIR, H<sub>2</sub>-TPR, O<sub>2</sub>-TPD, and XPS techniques. The NSR performance of LaCoO<sub>3</sub> perovskite was improved after Sr doping. Specifically, the perovskite with 50% of Sr doping (LS5 sample) exhibited excellent NO<sub>x</sub> storage capacity within a wide temperature range (200–400 °C), and excellent stability after hydrothermal and sulfur poisoning. It also displayed the highest NO<sub>x</sub> adsorption–storage capacity (NAC: 1889 μmol/g; NSC: 1048 μmol/g) at 300 °C. This superior performance of the LS5 catalyst can be attributed to its superior reducibility, better NO oxidation capacity, increased surface Co<sup>2+</sup> concentration, and, in particular, its generation of more oxygen vacancies. FTIR results further revealed that the LSX catalysts primarily store NO<sub>x</sub> through the “nitrate route”. During the lean–rich cycle tests, we observed an average NO<sub>x</sub> conversion rate of over 50% in the temperature range of 200–300 °C, with a maximum conversion rate of 61% achieved at 250 °C.

**Keywords:** perovskite oxides; NO<sub>x</sub> storage and reduction; strontium doping



**Citation:** Luan, X.; Wang, X.; Zhang, T.; Gan, L.; Liu, J.; Zhai, Y.; Liu, W.; Wang, L.; Wang, Z. NO<sub>x</sub> Storage and Reduction (NSR) Performance of Sr-Doped LaCoO<sub>3</sub> Perovskite Prepared by Glycine-Assisted

Solution Combustion. *Compounds* **2024**, *4*, 268–287. <https://doi.org/10.3390/compounds4020014>

Received: 15 January 2024

Revised: 26 March 2024

Accepted: 1 April 2024

Published: 8 April 2024



**Copyright:** © 2024 by the authors. Licensee MDPI, Basel, Switzerland. This article is an open access article distributed under the terms and conditions of the Creative Commons Attribution (CC BY) license (<https://creativecommons.org/licenses/by/4.0/>).

## 1. Introduction

Nitrogen oxides (NO<sub>x</sub>) are considered to be significant air pollutants generated in diverse combustion processes. Researchers have explored and recognized NO<sub>x</sub> storage and reduction (NSR) [1] and selective catalytic reduction (SCR) [2] as effective methods for removing NO<sub>x</sub> from exhaust emissions. NSR catalysts typically consist of active components such as noble metals (Pt, Pd, Rh) [3,4], storage components such as alkali or alkaline earth metals, and supports such as Al<sub>2</sub>O<sub>3</sub> or CeO<sub>2</sub> [5,6]. A representative catalyst commonly employed in NO<sub>x</sub> storage and reduction (NSR) systems is Pt-BaO/Al<sub>2</sub>O<sub>3</sub>. The operation of this catalyst involves alternating cycles of lean and rich conditions. Specifically, in the lean phase, the platinum (Pt) active sites facilitate the oxidation of NO to NO<sub>2</sub>. Following this conversion, the resulting NO<sub>2</sub> species are subsequently stored as nitrates and nitrites on the barium oxide (BaO) sites [7]. In the rich phase, the oxidation of NO<sub>x</sub> occurs, followed by its reduction to N<sub>2</sub> through the catalytic action of a reducing agent [8,9]. However, the use of Pt-based catalysts is limited due to their high cost, low activity at low temperatures [10], susceptibility to sintering at high temperatures, and poor resistance to sulfur [11]. Therefore, there is an urgent need to develop NSR catalysts with excellent low-temperature activity.

Perovskite ( $ABO_3$ ) catalysts have been widely employed in environmental catalysis due to their low cost, superior thermal stability, and catalytic activity [12]. Alkali or alkaline earth metals have the potential to act as substitutes for the A-site, while transition metals can replace the B-site in perovskite catalysts. Incorporation of alkali or alkaline earth metal dopants plays a vital role in controlling the performance of perovskite catalysts by facilitating the creation of more oxygen vacancies and stabilizing the perovskite structure. The study conducted by Ueda et al. [13] revealed that the incorporation of  $Ba^{2+}$  ions amounting to 30% into  $La^{3+}$ -based perovskite ( $LaFe_{0.97}Pd_{0.03}O_3$ ) remarkably tripled the capacity for  $NO_x$  storage. Similarly, Panunzi et al. [14] synthesized lanthanum strontium ferrite (LSFPt), and investigated how the oxygen vacancy content and the catalyst surface activity were enhanced in combined Sr substitution at the A-site and Pt doping at the B-site of lanthanum ferrites, leading to a substantial improvement in the activity and stability of methane oxidation. Concomitantly, Ji et al. [15] proposed that Sr dopants played a crucial role in enhancing the performance of catalysts during low-temperature reduction. Moreover, substitution of La with Sr in perovskite compounds like  $LaCoO_3$  and  $LaMnO_3$  exhibited enhanced oxidation activity, effectively converting NO to  $NO_2$  [16,17]. Thus, Sr doping at the A site in perovskite catalysts yields improved NO oxidation performance and thermal stability.

NSR for environmental catalysis is known to have various drawbacks associated with thermal aging and sulfur poisoning [18,19]. The catalytic materials are typically exposed to high temperature, resulting in sintering of active sites/promoters/catalytic support materials and loss of specific surface area (SSA) and functionality [20]. Furthermore, since acidic  $NO_2(g)$  and  $SO_2(g)$  adsorbates compete for similar adsorption sites on the catalyst surface,  $SO_x$  species gradually accumulate over the  $NO_x$ -storage components and form more stable sulfides, diminishing the NSC of the catalyst [21]. Therefore, the  $ABO_3$  surface chemistry and composition of catalytic materials need to be tuned at the nanoscale to improve their NSC, thermal stability, and resistance to sulfur neutrality.

In this study, we aimed to enhance the  $NO_x$  storage and reduction performance of  $LaCoO_3$  catalysts by Sr doping at the A-site. The solution combustion method was employed to prepare the oxide materials. This method is attractive and simple [22], as it produces pure, uniform, and crystalline products with the desired composition and structure. In this study, we employed a rational design strategy and optimized the synthesis process, leading to the successful synthesis of perovskite-type catalysts. Specifically,  $La_{1-x}Sr_xCo_{1-\lambda}O_{3-\delta}$  ( $x = 0, 0.1, 0.3, 0.5, 0.7$ ) catalysts were synthesized via the glycine-assisted solution combustion method. Our research focused on elucidating the influence of Sr doping on the NSR performance. Additionally, Infrared Spectroscopy (FTIR) was employed to analyze the  $NO_x$  storage route on the catalyst surface.

## 2. Experimental

### 2.1. Catalyst Preparation

The perovskite-type catalysts  $La_{1-x}Sr_xCoO_3$  ( $x = 0, 0.1, 0.3, 0.5, 0.7$ ) were synthesized using the glycine-assisted solution combustion method, denoted as LSX ( $X = 0, 1, 3, 5, 7$ ). The theoretical value of  $(La + Sr)/Co$  is set to 1:1. A precise amount of  $La(NO_3)_3 \cdot 6H_2O$ ,  $Co(NO_3)_2 \cdot 4H_2O$ , and  $Sr(NO_3)_2 \cdot 4H_2O$  was dissolved in deionized water. Following the addition of glycine ( $G/N = 1.6$ ) to the mixture of nitrates, the resulting solution was stirred at ambient temperature for a duration of 2 h. Subsequently, the solution underwent evaporation under constant stirring at  $80^\circ C$  until a viscous gel with a distinctive purple hue was obtained. The gel was combusted in an oven at  $200^\circ C$ . After the reaction was completed, the fluffy flocculent product was ground to a powder and calcined in a muffle furnace at  $700^\circ C$  for 4 h.

## 2.2. Catalysts Characterization

X-ray diffraction (XRD) patterns of the samples were obtained using the German D8 advance. The radiation source used was Cu K $\alpha$ . A scanning range of 10 to 90° was employed, with a scanning speed of 6° per minute.

The specific surface area, pore volume, and size of the samples were measured at −196 °C through utilization of an ASAP 2020 automated specific surface area and porosity analyzer. In preparation for the assessment, all samples were subjected to a 6 h vacuum degassing process at 300 °C to eliminate any adsorbed species. The surface areas of the samples were determined by employing the Brumauer–Emmett–Teller (BET) technique.

The surface morphology and microstructure of the specimens were examined utilizing a Quanta FEG 250 scanning electron microscope (Carl Zeiss AG, Oberkochen, Germany). The applied working voltage was 10 kV, and a thin layer of gold was deposited on the specimens for 60 s prior to the scanning process.

The infrared spectra (FTIR) of the specimens were recorded with a Bruker tensor 27 infrared spectrometer (Bruker, Saarbrücken, Germany) located in Germany. The spectra were acquired by conducting 16 scans at a resolution of 4 cm<sup>−1</sup>. Prior to the analysis, the specimens were mixed with dry KBr in a ratio of 1:100 and subsequently compressed into tablets using a tablet press under a pressure of 10 MPa.

Using a quartz tube reactor equipped with a TCD (thermal conductivity detector) (Lunan Ruihong Chemical, Zaozhuang, China), we conducted temperature-programmed reduction with H<sub>2</sub> (H<sub>2</sub>-TPR) measurements. The catalysts, weighing 0.05 g, were progressively heated from ambient temperature to 900 °C in the presence of a 5 vol.% H<sub>2</sub>/N<sub>2</sub> mixture. The heating rate was set at 10 °C per minute, while maintaining a total flow rate of 30 mL/min.

O<sub>2</sub> temperature-programmed desorption (O<sub>2</sub>-TPD) tests were conducted to observe the dynamic process of oxygen adsorption and desorption on perovskite. A quartz tube reactor with a capacity of approximately 150 mg of catalyst sample was utilized. The sample was subjected to a purification procedure involving a 30 min purge using a mixture of 10 vol% O<sub>2</sub> in N<sub>2</sub> flow (50 mL/min) at a temperature of 500 °C. Following the purification step, the sample was cooled to 50 °C and underwent an additional 30 min purge with N<sub>2</sub> flow (50 mL/min) to eliminate any residual adsorbed oxygen. Subsequently, a gradual heating process was conducted from 50 to 900 °C at a heating rate of 10 °C/min under a N<sub>2</sub> flow (30 mL/min), while simultaneously monitoring the released oxygen employing a TCD. Integration of the resulting TPD curves facilitated the determination of the quantities of oxygen species present.

By employing the Thermo Scientific X-ray photoelectron spectrometer (Bruker, Saarbrücken, Germany) equipped with an Al K $\alpha$  X-ray radiation source, we were able to precisely determine the chemical composition and oxidation states of surface elements in catalysts. To calibrate the binding energy measurements, we utilized the C1s peak (BE = 284.6 eV) as a reference standard.

## 2.3. Catalytic Activity Measurements

### 2.3.1. NO Oxidation Experiments

The investigation into the oxidation process of NO was conducted using the temperature-programmed oxidation (NO-TPO) technique. Prior to the experimentation, the catalysts underwent a pretreatment process involving exposure to N<sub>2</sub> at a temperature of 500 °C for a duration of one hour, followed by natural cooling to room temperature. Subsequently, the gas mixture was converted to contain 1000 ppm NO/N<sub>2</sub> and 5% O<sub>2</sub>/N<sub>2</sub>, and left to stabilize for a certain period. Finally, once the NO<sub>x</sub> concentration at the outlet remained constant, the temperature was increased to 700 °C at a rate of 5 °C per minute. The concentration of NO<sub>x</sub> was measured using a chemiluminescence NO<sub>x</sub> analyzer.

### 2.3.2. NO<sub>x</sub> Adsorption–Desorption Measurements

The catalysts (50 mg, 40–80 mesh) were examined for their NO<sub>x</sub> adsorption and storage capacity (NAC/NSC) using a custom-built catalyst sample evaluation system equipped with a chemiluminescence NO<sub>x</sub> analyzer (Thermo 42i–HL) (Thermo Fisher Scientific, Waltham, MA, USA). Initially, the feed gas was composed of 1000 ppm of NO and 5% O<sub>2</sub> for NO<sub>x</sub> adsorption, while N<sub>2</sub> was utilized as the balance gas. After adsorbing NO<sub>x</sub> for 1 h, the system was purged by introducing N<sub>2</sub> into the reaction chamber. Subsequently, the temperature was ramped up to 700 °C at a heating rate of 10 °C/min. The total flow rate was maintained at 100 mL/min. The LS5 catalyst after hydrothermal aging and sulfur poisoning was re-tested under the same conditions as those used for the fresh catalyst. The NAC/NSC was determined by calculating the NO<sub>x</sub> adsorption–desorption curves using Equations (1) and (2).

$$\text{NAC} = \left( \int_0^t (\text{NO}_{x,\text{in}} - \text{NO}_{x,\text{out}}) \times V \right) / (22.4 \times m_c) \quad (1)$$

$$\text{NSC} = \left( \int_0^t (\text{NO}_{x,\text{out}}) \times V \right) / (22.4 \times R \times m_c) \quad (2)$$

where NO<sub>x,in</sub> is the NO<sub>x</sub> concentration at the inlet, NO<sub>x,out</sub> is the NO<sub>x</sub> concentration at the outlet, *t* is time, *V* is the flow rate, *m<sub>c</sub>* is the catalyst quantity, and *R* is the heating rate.

### 2.3.3. NO<sub>x</sub> Storage and Reduction Measurements

To assess the efficiency of catalysts in reducing NO<sub>x</sub> emissions, a comprehensive array of NO<sub>x</sub> storage and reduction experiments was executed, spanning diverse temperature ranges. The experimental design entailed 15 cycles, wherein each lean phase persisted for 2 min, incorporating a gas mixture comprising 500 ppm of NO/N<sub>2</sub> and 7.5 vol.% of O<sub>2</sub>/N<sub>2</sub>. Conversely, the rich phase spanned 1 min, during which a gas composition of 500 ppm of NO/N<sub>2</sub> and 1200 ppm of C<sub>3</sub>H<sub>8</sub>/He was employed. The overall volumetric flow rate was consistently maintained at 50 mL/min (GHSV: 60,000 h<sup>−1</sup>). The chemiluminescence NO<sub>x</sub> analyzer was used to measure the NO<sub>x</sub> concentration at the outlet, and subsequently, the NO<sub>x</sub> removal efficiency of the catalysts was determined using Equation (3).

$$\text{NO}_x \text{ conversion (\%)} = \frac{\int_0^t (\text{NO}_{x,\text{in}} - \text{NO}_{x,\text{out}}) dt}{\int_0^t (\text{NO}_{x,\text{in}}) dt} \cdot 100\% \quad (3)$$

## 3. Results and Discussion

### 3.1. XRD Analysis

The XRD patterns of LSX perovskite catalysts are illustrated in Figure 1a. Pure perovskite diffraction patterns were obtained with Sr doping amounts lower than 30%, indicating the absence of impurities. However, after Sr doping reached 50%, trace amounts of impurities in the form of SrCO<sub>3</sub> and SrCoO<sub>x</sub> were detected on the LS5 catalyst. In addition, the impurity phase SrCoO<sub>x</sub> was distinctly observed on the LS7 sample. Therefore, it can be concluded that the LS5 catalyst allows for higher Sr accommodation in the lattice compared to the LS7 catalyst. The cobalt in perovskite serves as the active oxidation site [23], while the hybrid SrCoO<sub>x</sub> species may occupy the LS7 catalyst surface and cover the active component, thereby influencing the catalyst activity.

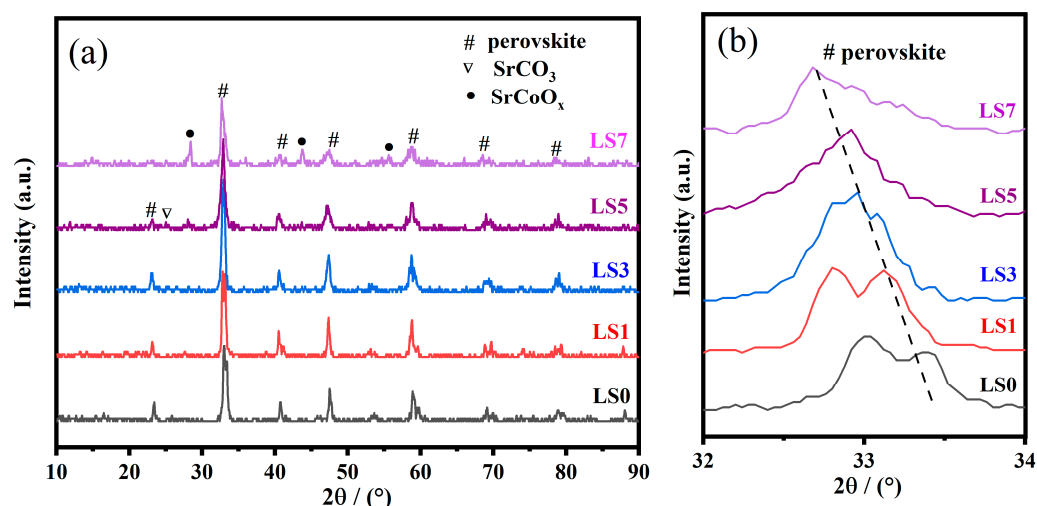


**Figure 1.** (a) XRD and (b) the peak of crystal plane (110) of LSX catalysts.

An enlarged version of the peak from the crystal plane (110) of LSX perovskite catalysts is presented in Figure 1b. The peak of the crystal plane (110) shifts to a lower  $2\theta$  angle as the Sr doping content increases. This shift is caused by lattice expansion resulting from the isomorphous substitution of  $\text{Sr}^{2+}$  cations with larger ionic radii replacing  $\text{La}^{3+}$  ions. Furthermore, the LSX catalysts exhibit a rhomboid bimodal structure in the absence of, or with low, strontium doping ( $X \leq 1$ ) [24]. As the Sr doping content increases, this typical rhomboid bimodal structure weakens and gradually transforms into a cubic symmetric singlet structure [25].

### 3.2. SEM and EDS Mapping Analysis

The scanning electron microscope (SEM) images of LS0 and LS5 catalysts are presented in Figure 2a,b. Both catalysts exhibit similar loose and porous spongy morphological structures, both before and after Sr doping. The formation of abundant pores can be attributed to the release of  $\text{CO}_2$ ,  $\text{N}_2$ , and  $\text{H}_2\text{O}$  during the combustion of the precursor materials [26,27]. This porous structure enhances the dispersion, absorption, and desorption of gas reactants. However, there are differences in grain size and dispersion between the two catalysts, which can be attributed to the variation in Sr doping. The LS5 catalyst has smaller particle diameters and appears to be in a looser state. A smaller grain size provides more catalytic active sites, leading to higher catalytic activity.

The energy-dispersive X-ray spectroscopy (EDS) mapping of LS0 and LS5 catalysts is shown in Figure 2c,e, revealing the uniform distribution of La, Sr, Co, and O atoms across their respective surfaces. Furthermore, the distribution diagram depicted in Figure 2d,f facilitates the determination of the  $(\text{La} + \text{Sr})/\text{Co}$  ratio on the catalyst surfaces, which aligns with the theoretical outcomes as illustrated in Table 1.

**Table 1.** Textural parameters for  $S_{\text{BET}}$ ,  $V_p$ , and  $D_p$  of the LSX catalysts.

Catalyst	$S_{\text{BET}}$ ( $\text{m}^2/\text{g}$ )	$V_p$ ( $\text{cm}^3/\text{g}$ )	$D_p$ (nm)	Mesopore Fraction	$(\text{La} + \text{Sr})/\text{Co}$
LS0	5.58	0.05	41	0.36	1.20
LS1	12.38	0.08	32	0.66	-
LS3	13.44	0.13	29	0.76	-
LS5	17.71	0.11	22	0.75	1.09
LS7	15.96	0.09	23	0.70	-

(La + Sr)/Co: EDS results; Mesopore Fraction: Percentage of mesopore to total pore;  $D_p$ : Average Pore diameter.

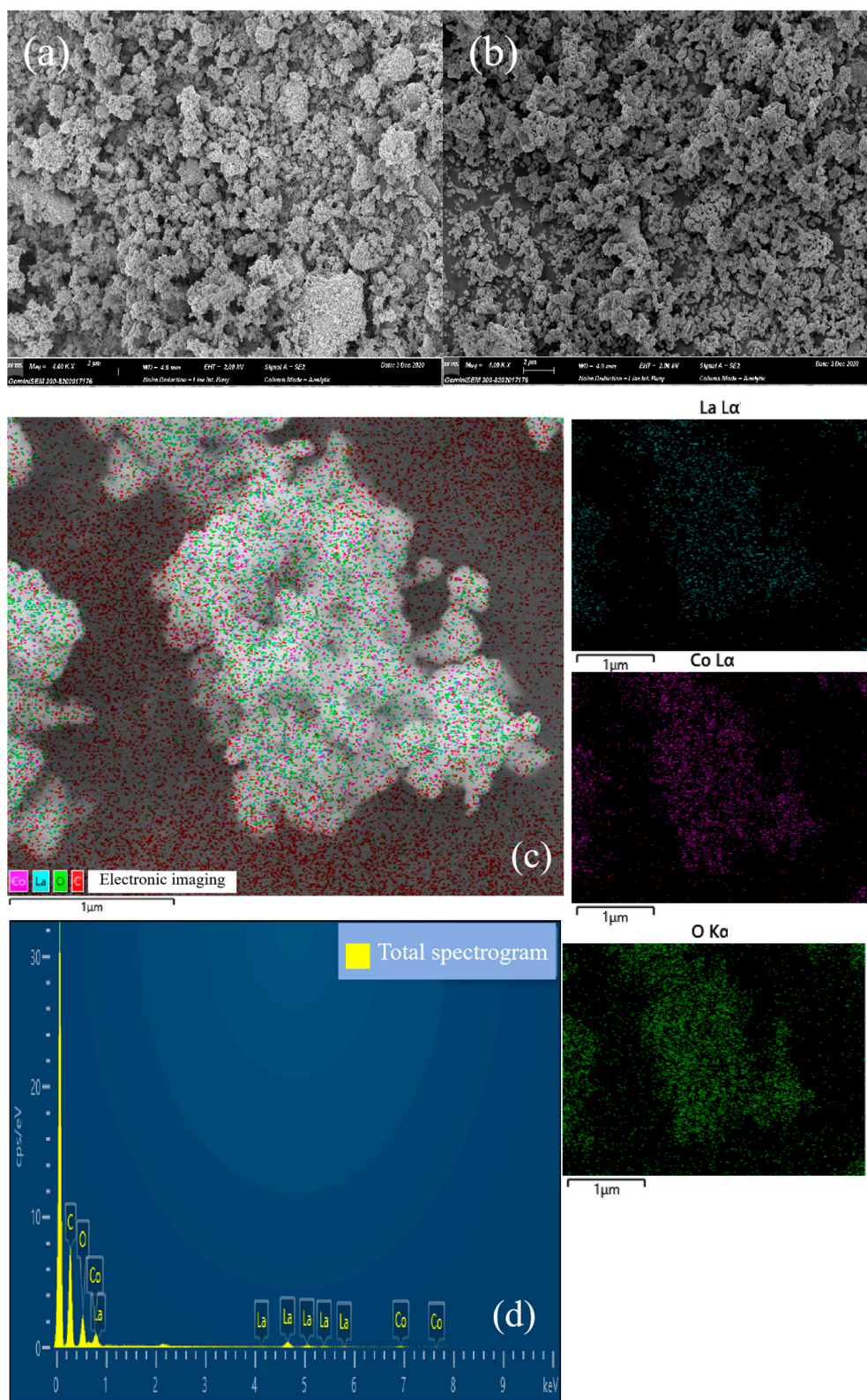
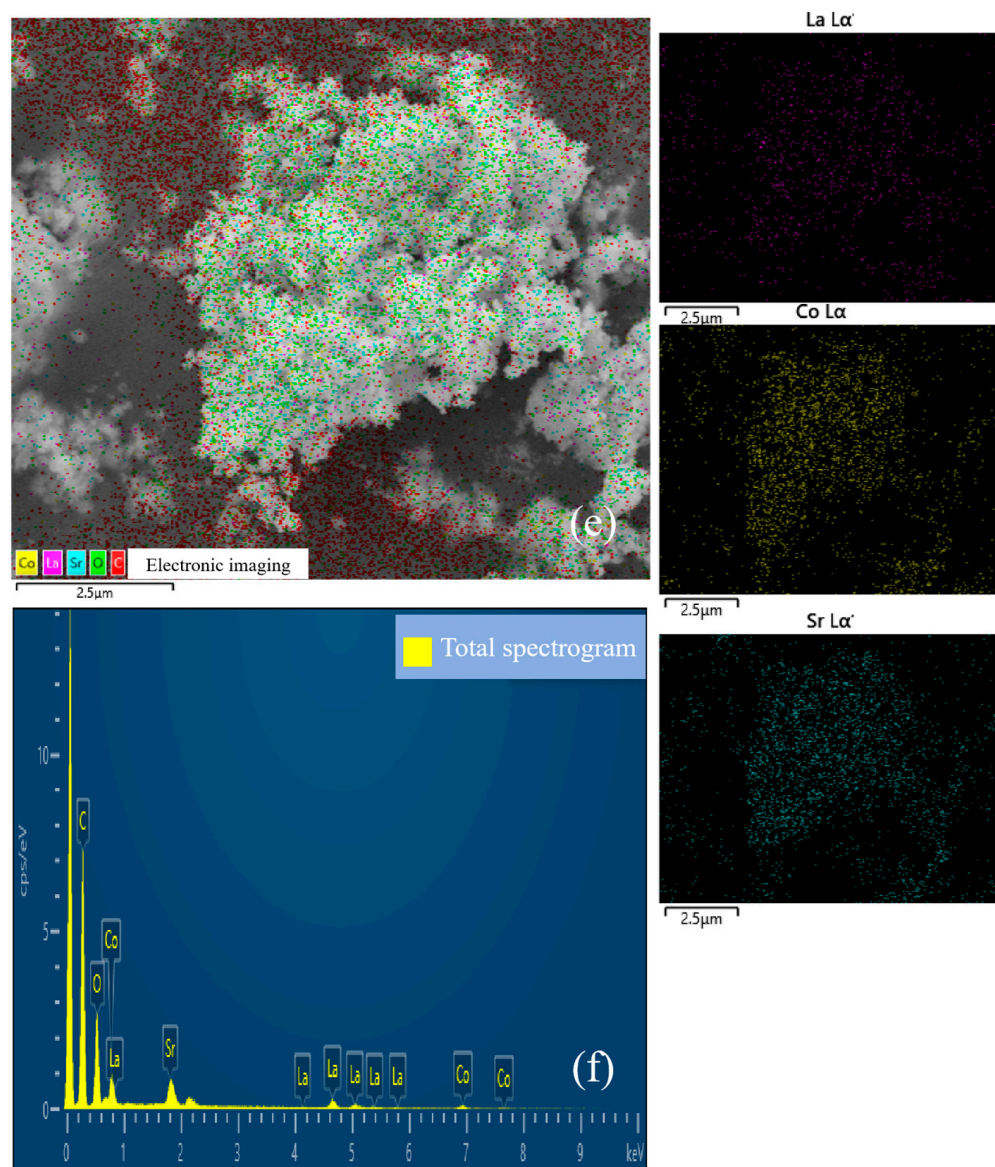


Figure 2. Cont.



**Figure 2.** SEM and EDS mapping images of (a,c,d) LS0 and (b,e,f) LS5 catalysts.

### 3.3. $N_2$ Adsorption–Desorption Analysis

The  $N_2$  adsorption–desorption curves of the samples are depicted in Figure 3a. All catalysts exhibit IUPAC type II isotherms, and a H3 type hysteresis loop is observed in the range of  $p/p_0 = 0.8–1.0$ , indicating the presence of macroporous materials [28]. The pore size distribution curve in Figure 3b combined with SEM images reveals that all catalysts possess a multistage pore structure consisting of both mesopores and macropores.

In Table 1, the LSX catalysts are characterized by their BET surface areas ( $S_{BET}$ ), pore volume ( $V_p$ ), and average pore size ( $D_p$ ). Among them, the LS0 sample possesses the smallest surface area of  $5.58 \text{ m}^2/\text{g}$  and a corresponding pore volume of  $0.05 \text{ cm}^3/\text{g}$ . Through Sr doping, the LSX catalysts exhibit an increasing trend in both surface area and pore volume with the escalating Sr doping amount, while the pore size demonstrates the opposite relationship. The LS5 sample demonstrates the largest surface area of  $17.71 \text{ m}^2/\text{g}$ , coupled with a pore volume of  $0.11 \text{ cm}^3/\text{g}$ . However, as the Sr doping content further rises ( $X = 7$ ), LS7 experiences a slight reduction in both surface area and pore volume. This may be due to impurities, such as  $\text{SrCoO}_x$  and  $\text{SrCO}_3$ , which block the catalyst's pores and affect its textural parameters. Previous studies [29,30] have proposed that optimizing the pore structure by reducing its size can significantly improve gas transport properties and

boost catalytic activity. Furthermore, Table 1 reveals that Sr doping significantly increases the mesoporous rate of the catalysts, leading to a larger surface area in the corresponding samples. This larger surface area exposes more active sites, facilitating contact between the catalyst and gas, and thus improving reaction efficiency [31].

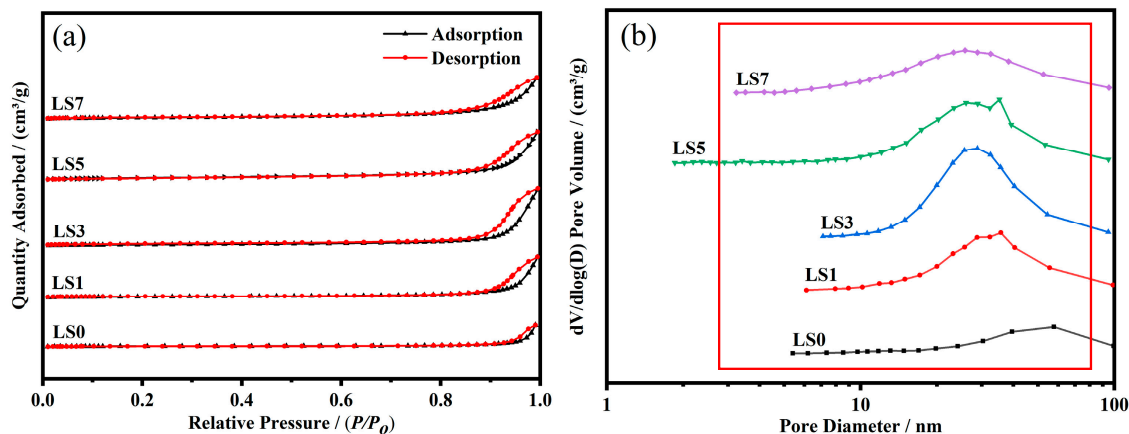


Figure 3. (a) N<sub>2</sub> adsorption–desorption curves and (b) pore size distributions of LSX catalysts.

### 3.4. FTIR and H<sub>2</sub>-TPR Analysis

The FTIR spectra of the LSX catalysts are presented in Figure 4a. Among the catalysts with varying amounts of Sr doping, it is observed that the bending vibration of Co-O bonds in the octahedral structure of perovskite BO<sub>6</sub> is assigned to approximately 580 cm<sup>-1</sup> [32]. This suggests the successful preparation of the perovskite structure. Additionally, the peaks at 858 and 1451 cm<sup>-1</sup> are attributed to surface carbonate [33,34]. When considering the XRD results, it is further confirmed that SrCoO<sub>3</sub> exists in the samples. Comparing the catalysts before and after Sr doping, it is evident that the characteristic peak of perovskite is significantly weakened upon the introduction of Sr, indicating that Sr has a certain impact on the integrity of the perovskite crystal.

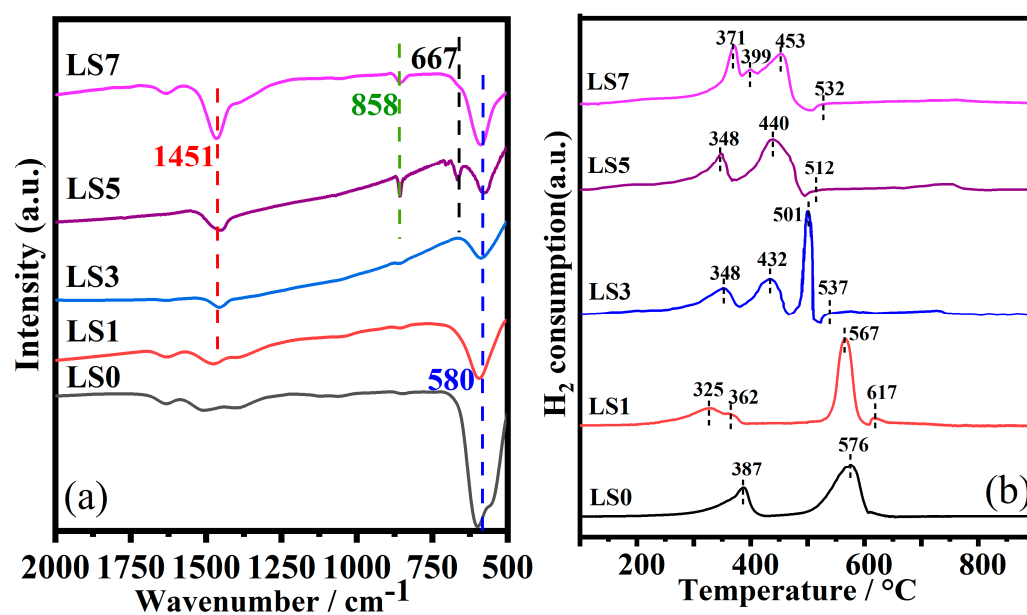


Figure 4. (a) FTIR spectra and (b) H<sub>2</sub>-TPR profiles of the LSX catalysts.

The reducibility of the LSX samples was assessed via H<sub>2</sub>-TPR, as depicted in Figure 4b. The peaks observed in the temperature range of 100 °C to 800 °C can all be attributed solely to the reduction of Co<sup>3+</sup>. This finding is consistent with the notion that La<sup>3+</sup> and Sr<sup>2+</sup> are impervious to reduction under the specific experimental conditions employed [24]. In all catalysts, the reduction peaks witnessed in the 300–430 °C range correspond to the reduction of Co<sup>3+</sup>, whereas those observed within the 440–620 °C range align with the reduction of Co<sup>2+</sup> [35,36]. Specifically, between 300 and 430 °C, there are two reduction peaks for Co<sup>3+</sup> with  $x > 1$ . The peak at the lower temperature is related to surface/highly reactive Co<sup>3+</sup>, which is in accordance with the stepwise reduction behavior of fine Co<sub>3</sub>O<sub>4</sub> particles [37]. Notably, the reduction temperature of Co species on the doped catalysts exhibits a noticeable decrease compared to that of the undoped catalyst when the Sr doping level is maintained below 50%. This noteworthy trend alludes to the beneficial influence of Sr doping, which serves to enhance the reduction performance of the catalysts and facilitate the reduction of surface oxygen [24]. However, when  $X \geq 5$ , the intensity of the reduction peak in the range of 500–540 °C decreased significantly. Combined with the XRD results, it is speculated that the reason for this occurrence may be the inhibitory effect of the presence of SrCoO<sub>x</sub> and SrCO<sub>3</sub> impurities on the reduction of Co<sup>2+</sup>. Furthermore, exceeding a certain threshold of Sr doping leads to a slight elevation in the reduction temperature of Co species, signifying that excessive Sr doping does not favor the reduction process of the catalysts.

The H<sub>2</sub> consumption of all samples is listed in Table 2. It can be concluded that Sr doping increases the H<sub>2</sub> consumption of the catalysts. Noticeably, the LS3 catalyst possesses the highest H<sub>2</sub> consumption (8.1 mmol/g), followed by the LS5 catalyst (7.5 mmol/g). The result shows that LS3 and LS5 catalysts have better reducibility.

**Table 2.** H<sub>2</sub>-TPR and O<sub>2</sub>-TPD results.

Catalyst	H <sub>2</sub> Consumption (mmol/g)	Peak Area	
		$\alpha$ -Peak	$\beta$ -Peak
LS0	5.7	100	-
LS1	6.2	177	39
LS3	8.1	194	369
LS5	7.5	219	578
LS7	6.9	172	668

### 3.5. O<sub>2</sub>-TPD

O<sub>2</sub> temperature-programmed desorption tests were conducted on the LSX catalysts and the results are presented in Figure 5. The integral areas of the  $\alpha$  and  $\beta$  peaks were determined from the O<sub>2</sub>-TPD spectra, as shown in Table 2. Except for LS0, all LSX catalysts exhibited a  $\alpha$ -oxygen desorption peak below 300 °C and a  $\beta$ -oxygen desorption peak above 600 °C. The  $\alpha$ -peak in the graph represents the desorption of surface-adsorbed oxygen (O<sup>2-</sup>) species, whereas the  $\beta$ -peak corresponds to the liberation of lattice oxygen (O<sup>2-</sup>) ions [38]. The graph displays an upsurge in the intensity of the  $\alpha$ -peak during Sr doping, indicating that Sr doping facilitates the desorption of surface oxygen species. Typically, an increase in the concentration of oxygen species associated with the  $\alpha$ -peak enhances catalytic activity [12]. Among the catalysts, LS5 demonstrated the lowest  $\alpha$ -peak temperature of 118 °C and the largest peak area, indicating a higher concentration of surface oxygen species and stronger oxidation properties. Furthermore, the intensity of the  $\beta$ -oxygen desorption peak increased with Sr doping, with the maximum observed for the LS7 catalyst.

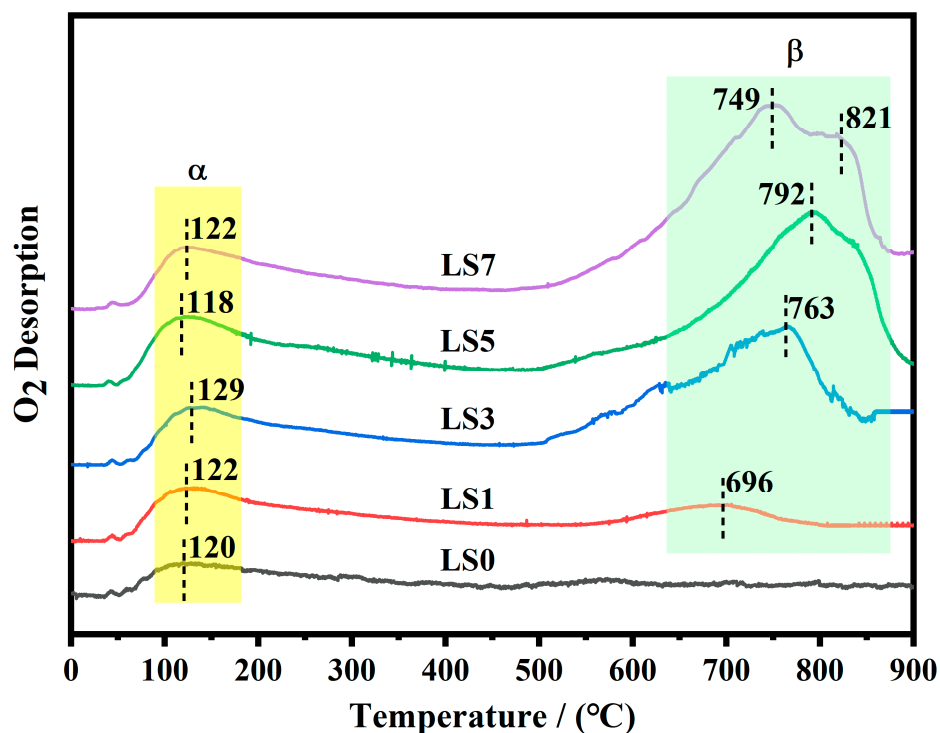


Figure 5. O<sub>2</sub>-TPD spectra of the LSX catalysts.

### 3.6. XPS

The surface properties of the synthesized LSX catalysts were confirmed using X-ray photoelectron spectroscopy (XPS), as illustrated in Figure 6. The Sr 3d XPS peak exhibited two distinct sets of doublets, specifically Sr 3d<sub>5/2</sub> and 3d<sub>3/2</sub>. The peaks observed at binding energies of 131.7 and 134.1 eV can be assigned to Sr<sub>latt</sub>, while the peaks detected at 133.1 and 135.2 eV can be attributed to Sr<sub>surf</sub> [11,39]. The ratios of Sr<sub>surf</sub>/Sr<sub>latt</sub> are summarized in Table 1. The proportion of Sr<sub>surf</sub> increases with an increase in Sr doping. It is likely that Sr<sub>surf</sub> species are present in the form of SrCO<sub>3</sub>, as suggested by XRD and FTIR results. An increase in the amount of Sr<sub>surf</sub> signifies an increase in the content of SrCO<sub>3</sub>. This is significant because SrCO<sub>3</sub> is an important storage phase for NO<sub>x</sub> adsorption, suggesting that the LS5 catalyst may possess a strong capacity for NO<sub>x</sub> adsorption and storage.

The Co 2p XPS peak was fitted with two sets of Co 2p<sub>3/2</sub> and 2p<sub>1/2</sub> doublets. The peaks at 779.7 and 794.9 eV were assigned to Co<sup>3+</sup>, while the peaks at 781 and 796.5 eV were attributed to Co<sup>2+</sup>. The peaks at 790 and 804 eV were considered satellite peaks [40,41]. The bands of the fitted O1s spectra at 528.8–529.1 eV, 530.3–531.5 eV, and 533.0–533.8 eV could be assigned to lattice oxygen (O<sub>I</sub>), surface reactive oxygen (O<sub>II</sub>), and chemisorbed water (O<sub>III</sub>), respectively [42]. Table 3 presents the (La + Sr)/Co, Co<sup>2+</sup>/Co<sup>3+</sup>, and O<sub>II</sub>/(O<sub>I</sub> + O<sub>II</sub> + O<sub>III</sub>) ratios. The (La + Sr)/Co ratio increases with the decrease in the Sr doping amount, indicating that Sr doping results in the partial bulk Co ion segregation on the LSX surface. The high value of the (La + Sr)/Co ratio can be attributed to various reasons, one of which is the significant variation in this molar ratio from one site to another. This variation is caused by the swift application of high power densities, which leads to a highly heterogeneous structure [43]. As a result, there are abrupt changes in the (La + Sr)/Co values, both chemically and morphologically [44]. Therefore, this change is denoted by “1 – λ” in La<sub>1–x</sub>Sr<sub>x</sub>Co<sub>1–λ</sub>O<sub>3–δ</sub>. The quantities of both Co<sup>2+</sup> cations and O<sub>II</sub> species also increase with the Sr doping content. Notably, the LS3 catalyst exhibits the highest number of reactive oxygen species on its surface. This suggests that the content of reactive oxygen does not completely determine the activity of the catalysts. It has been shown that the oxygen vacancy is formed on the site of oxygen, coupled with cobalt [45]. Therefore, variations in O<sub>II</sub> fractions may be due to differences in oxygen vacancies or defects on the sample

surface, or differences in oxygen-deficient regions in the cobalt-containing structures [46]. Changes in the concentration of oxygen vacancies or defects in the sample may favor the chemisorption process. The LS5 catalyst contains a higher amount of surface  $\text{Co}^{2+}$ , which leads to the formation of oxygen vacancies and improves the NO oxidation capacity of the catalyst, thereby enhancing the  $\text{NO}_x$  storage performance.

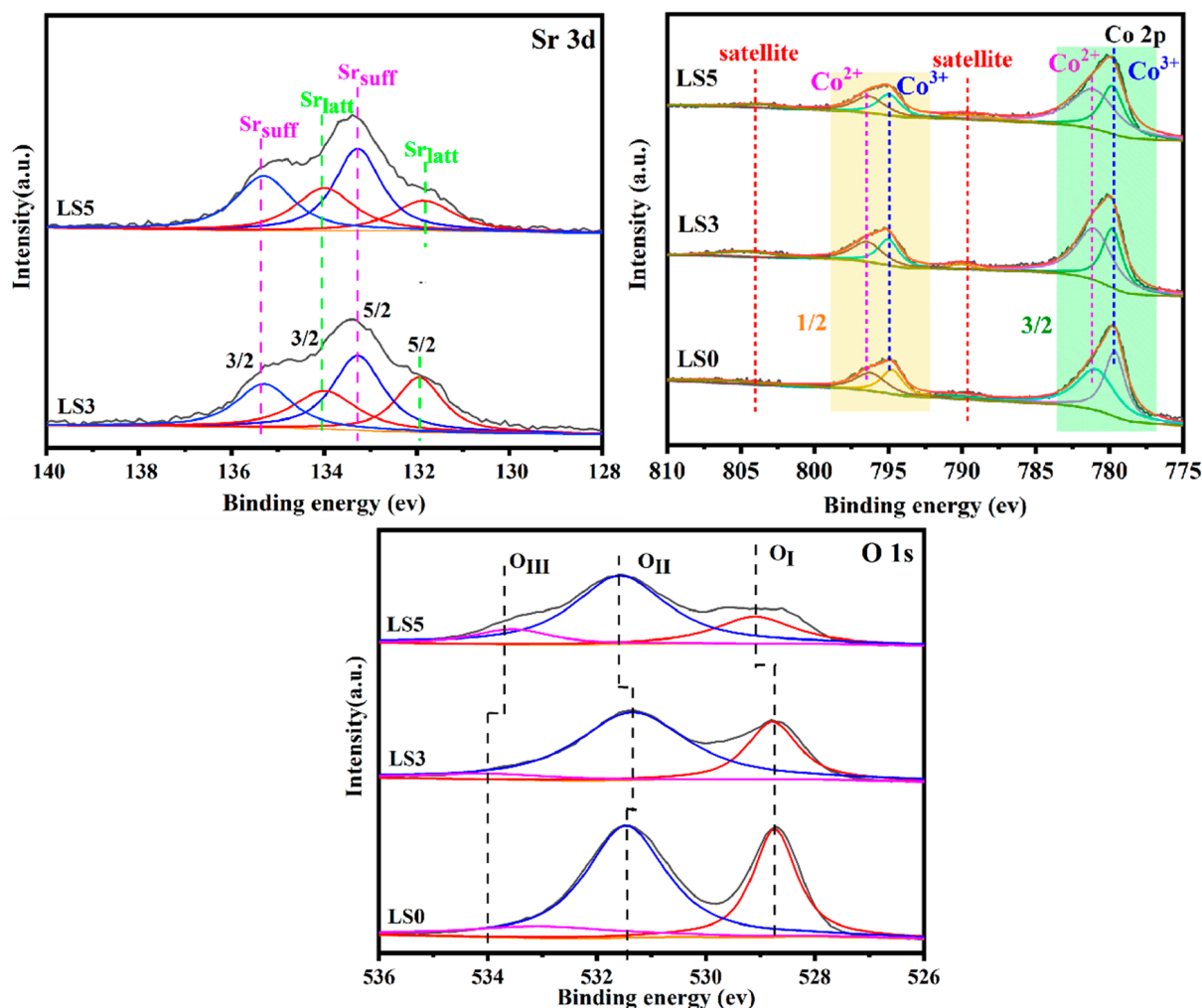


Figure 6. Sr 3d, Co 2p, O 1s XPS spectra of the LSX catalysts.

Table 3. XPS results.

Catalyst	$\text{O}_{\text{II}}/(\text{O}_{\text{I}} + \text{O}_{\text{II}} + \text{O}_{\text{III}})$ (%)	$\text{Co}^{2+}/\text{Co}^{3+}$	(La + Sr)/Co	$\text{Sr}_{\text{surf}}/\text{Sr}_{\text{latt}}$
LS0	57.6	1.13	2.33	-
LS3	68.6	1.41	1.28	1.23
LS5	65.8	1.43	1.05	1.6

$\text{O}_{\text{I}}$ : lattice oxygen;  $\text{O}_{\text{II}}$ : surface-active oxygen;  $\text{O}_{\text{III}}$ : Chemical adsorption of oxygen in water;  $\text{Sr}_{\text{latt}}$ : Sr lattice components;  $\text{Sr}_{\text{surf}}$ : Sr surface components.

### 3.7. NO Oxidation

The  $\text{NO}_x$  storage capacity of non-noble metal catalysts is subject to the influence of their NO oxidation capability [47]. The temperature-programmed oxidation of NO was conducted on LSX catalysts and the corresponding results are illustrated in Figure 7. The presence of the catalysts facilitates the conversion of NO to  $\text{NO}_2$  through oxidation reactions. Remarkably, even at temperatures as low as 100–150 °C, a considerable fraction of NO,

amounting to approximately 15%, can be converted into  $\text{NO}_2$ . The LSX catalysts reach their peak NO conversions within the temperature range of 300–365 °C. As the temperature continues to rise, the decline in NO conversion can be attributed to the thermodynamic equilibrium associated with NO oxidation. Notably,  $\text{LaCoO}_3$  exhibits remarkable catalytic activity towards NO oxidation, resulting in a peak conversion rate of 49.5% at 365 °C. The achievement of a higher conversion rate at a lower peak temperature indicates an enhanced capability for NO oxidation. Based on the data presented in Figure 7, it can be deduced that Sr doping enhances the NO oxidation capability of the catalysts, leading to a conversion rate surpassing 50%. Among the catalysts examined, LS3 demonstrates the optimal NO oxidation ability, achieving a maximum conversion rate of 76.8% at 305 °C. This observation can be attributed to an elevated presence of surface oxygen species and  $\text{Co}^{2+}$  in LS3. The generation of a substantial amount of  $\text{NO}_2$  during  $\text{NO}_x$  adsorption proves advantageous for adsorption via the “nitrate” pathway [48].

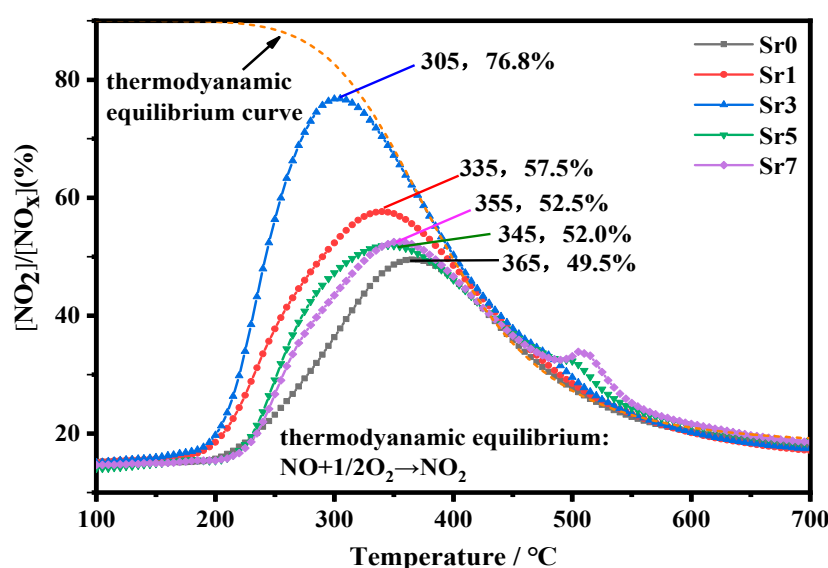
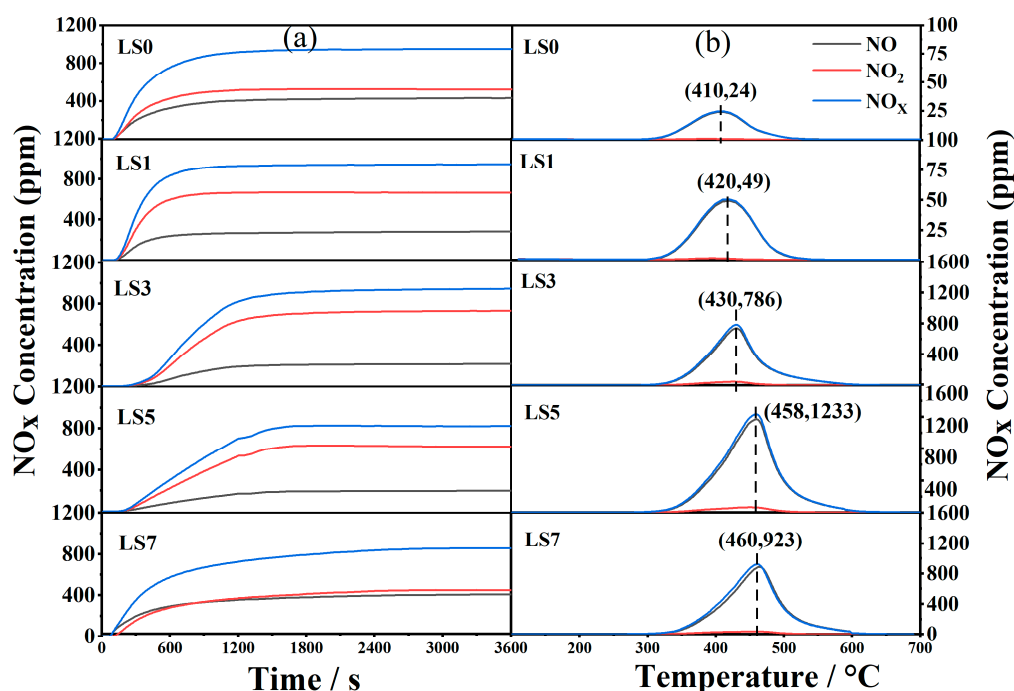


Figure 7. Oxidation curves of NO on the LSX catalysts.

### 3.8. $\text{NO}_x$ Adsorption/Storage Capacity

To assess the impact of Sr doping on the efficiency of  $\text{NO}_x$  storage, experiments were conducted to measure the adsorption and desorption of  $\text{NO}_x$  at a temperature of 300 °C. The results are presented in Figure 8. The adsorption curve (Figure 8a) clearly demonstrates that at the initial stage of adsorption,  $\text{NO}_x$  is almost entirely adsorbed. As adsorption progresses, the concentration of  $\text{NO}_x$  at the outlet gradually increases and stabilizes, suggesting that  $\text{NO}_x$  adsorption reaches saturation. Throughout this process,  $\text{NO}_2$  is detected at the outlet, indicating the oxidation of NO to  $\text{NO}_2$ . Previous studies have indicated that  $\text{NO}_2$  can be readily stored in the form of nitrate, and the conversion of NO to  $\text{NO}_2$  is the rate-determining step for  $\text{NO}_x$  storage in Pt/BaO/ $\text{Al}_2\text{O}_3$  catalysts [49]. Figure 8b illustrates the desorption behavior of the LSX catalysts. All catalysts exhibit a one-step desorption process. With increasing Sr doping content, the desorption peak of the catalysts shifts to higher temperatures, indicating that the addition of more strontium to perovskite leads to greater stability of the nitrate species.



**Figure 8.** (a) NO<sub>x</sub> adsorption curves and (b) desorption curves (at 300 °C) of the LSX catalysts.

Table 4 provides the data for the NO<sub>x</sub> adsorption capacity (NAC) and NO<sub>x</sub> storage capacity (NSC) of the LSX catalysts, as determined from their NO<sub>x</sub> adsorption–desorption profiles. It is important to note that the NAC and NSC show significant increases after Sr doping, suggesting that Sr enhances the storage of NO<sub>x</sub>. Additionally, both the NAC and NSC of the catalysts increase with higher levels of Sr doping ( $X \leq 5$ ). Among the catalysts, LS5 exhibits the highest adsorption and storage capacity, with an NAC of 1889  $\mu\text{mol/g}$  and an NSC of 1084  $\mu\text{mol/g}$ . This can be attributed to its larger surface area, strong reducibility, excellent NO oxidation activity, and the charge imbalance caused by Sr doping at the A-site, which promotes the generation of more active Co<sup>2+</sup> cations and surface reactive oxygen species [24]. However, when Sr doping continues to increase, the NAC and NSC of the catalysts decrease. This is likely due to an excessive amount of Sr doping, which results in the formation of large amounts of SrCO<sub>3</sub> and SrCoO<sub>x</sub>. These heterogeneous compounds do not disperse well on the surface, and the presence of a significant quantity of SrCoO<sub>x</sub> reduces the availability of effective storage sites and active sites, ultimately weakening the storage capacity of the catalysts.

**Table 4.** NAC and NSC of the LSX catalysts at 300 °C.

Catalysts	NAC ( $\mu\text{mol/g}$ )	NSC ( $\mu\text{mol/g}$ )
LS0	831	23
LS1	865	48
LS3	1485	635
LS5	1889	1084
LS7	1556	810

Wang et al. [50] developed LaCo<sub>0.90</sub>Pt<sub>0.10</sub>O<sub>3</sub> catalysts based on chalcogenides. These catalysts achieved a maximum NSC of 22.6  $\mu\text{mol/g}$  at 300 °C. Additionally, Wen et al. [51] studied the impact of adding LaCoO<sub>3</sub> chalcogenide to 1 wt% Pt/LaCoO<sub>3</sub>/K/Al<sub>2</sub>O<sub>3</sub> on NSR performance. Their results showed that a maximum NSC of 44.8  $\mu\text{mol/g}$  could be achieved at 400 °C. Furthermore, Xie et al. [52] tested the catalytic performance of LaCoO<sub>3</sub>-Meso with a high surface area in the NSR reaction. LaCoO<sub>3</sub>-Meso demonstrated a

maximum NSC of 124  $\mu\text{mol/g}$  at 300  $^{\circ}\text{C}$ . Although this is only a rough comparison of the data, it still demonstrates the superiority of the LS5 catalyst in terms of  $\text{NO}_x$  adsorption/storage capacity.

Based on the above studies, it was observed that the LS5 catalyst demonstrates remarkable performance in  $\text{NO}_x$  storage. Therefore, an investigation into its  $\text{NO}_x$  storage capabilities at varying adsorption temperatures (200–400  $^{\circ}\text{C}$ ) was conducted. The findings are presented in Figure 9. Initially, the LS5 catalyst completely traps NO, resulting in minimal  $\text{NO}_x$  levels. However, as the reaction time increases, the concentration of  $\text{NO}_x$  gradually rises until it reaches a certain threshold. Based on the  $\text{NO}_x$  concentration at the outlet, the conversion rate of NO can be calculated and is shown in Table 5: 300  $^{\circ}\text{C}$  (63%) > 250  $^{\circ}\text{C}$  = 350  $^{\circ}\text{C}$  = 400  $^{\circ}\text{C}$  (42%) > 200  $^{\circ}\text{C}$  (30%). Analysis of the  $\text{NO}_x$  desorption curve reveals that catalyst desorption follows a one-step process at different temperatures. Moreover, the desorption peak of the catalysts shifts to higher temperatures with increasing temperature. This suggests that elevating the temperature enhances the stability of nitrate.

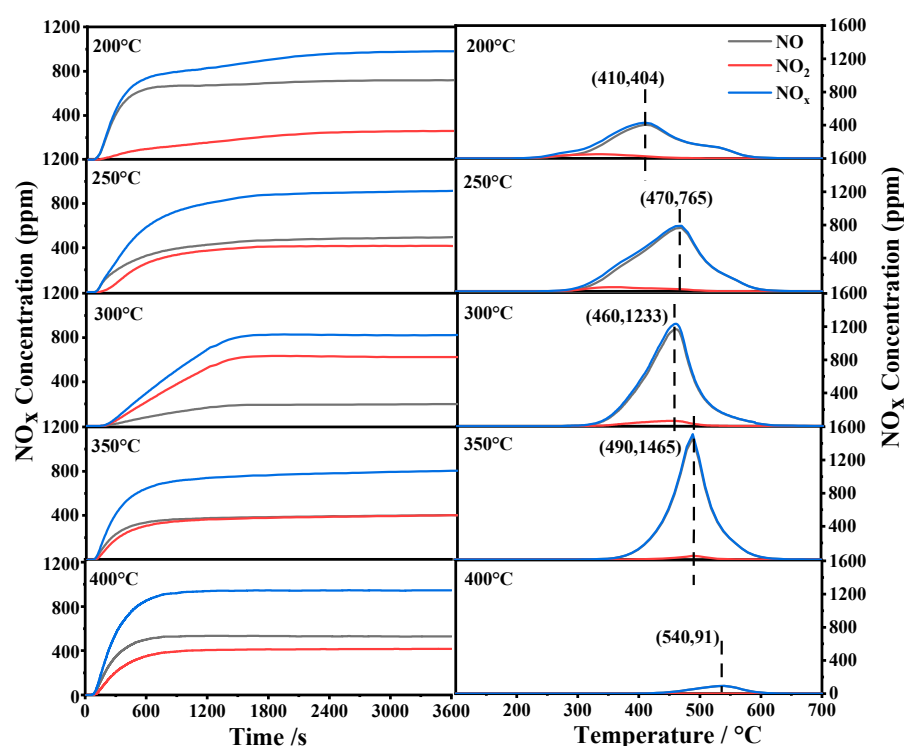


Figure 9.  $\text{NO}_x$  absorption–desorption curves of the LS5 catalyst at different temperatures (200–400  $^{\circ}\text{C}$ ).

Table 5. NAC, NSC, and  $R_{\text{NO}_2}$  at different adsorption temperatures on the LS5 catalyst.

Adsorption Temperature ( $^{\circ}\text{C}$ )	NAC ( $\mu\text{mol/g}$ )	NSC ( $\mu\text{mol/g}$ )	$R_{\text{NO}_2}$ (%)
200	937	609	30
250	1297	984	42
300	1889	1084	63
350	1633	1007	42
400	750	80	42

$R_{\text{NO}_2}$ : NO to  $\text{NO}_2$  conversion after reaching a steady state during the adsorption process.

The NAC and NSC of the LS5 catalysts were presented in Table 5. The catalyst's NAC and NSC reach their maximum values at 300  $^{\circ}\text{C}$ . However, as the adsorption temperature increases, the capacity for  $\text{NO}_x$  adsorption/storage decreases due to the exothermic nature of the process [48].

To investigate the impact of hydrothermal aging and sulfur on the NO<sub>x</sub> storage performance of LS0 and LS5 catalysts, experiments were performed to analyze NO<sub>x</sub> adsorption and desorption at 300 °C. Tables 6 and 7 summarize the NO<sub>x</sub> adsorption capacity and R<sub>NO2</sub> of LS0 and LS5 catalysts. The results reveal that the presence of water reduces the catalyst's acidity after hydrothermal aging, leading to decreased efficiency in NO to NO<sub>2</sub> conversion and a subsequent loss in NO<sub>x</sub> storage performance. However, perovskite promotes Sr dispersion and stability during hydrothermal aging, mitigating negative effects on the catalyst. The presence of impurities SrCoO<sub>x</sub> and SrCO<sub>3</sub> also affected the NO<sub>x</sub> storage performance of the catalysts. It is hypothesized that hydrothermal aging increases the likelihood of SrCoO<sub>x</sub> and SrCO<sub>3</sub> production, which has a reverse effect on catalysis. Moreover, the smaller decrease in NAC of Sr-doped catalysts suggests that Sr doping enhances the hydrothermal resistance of the catalysts. Table 7 depicts the effect of sulfur on the LS0 and LS5 catalysts. The NAC decrease rate of the LS5 sample is lower than that of the LS0 sample. This may be because Sr completely enters the perovskite lattice in the LS0 catalyst. After the introduction of SO<sub>2</sub>, SO<sub>2</sub> directly poisons perovskite. However, in the LS5 catalyst, Sr exists in the form of perovskite and SrCO<sub>3</sub>, and after the introduction of SO<sub>2</sub>, SO<sub>2</sub> easily reacts with SrCO<sub>3</sub>. This weakens the toxicity of the perovskite structure, resulting in a small decrease in the NAC of the catalysts. This indicates that Sr doping enhances the sulfur-resistant performance of the LS5 catalyst. Additionally, Sr doping increases the specific surface area, which supports better dispersion of the storage sites. Therefore, the small amount of sulphate species generated by the reaction of SO<sub>2</sub> with SrCO<sub>3</sub> is not sufficient to completely inactivate the NO<sub>x</sub> storage sites of the catalyst. This is another reason for the superior NO<sub>x</sub> storage performance of the sulfided LS5 chalcogenide catalyst.

**Table 6.** Comparison of NAC and R<sub>NO2</sub> after hydrothermal aging of LS0 and LS5 catalysts.

Catalyst	NAC (μmol/g)		R <sub>NO2</sub>		The Decline Rate of NAC
	Fresh	Hydrothermal Aging	Fresh	Hydrothermal Aging	
LS0	831	461	52	33	44.5
LS5	1889	1262	63	38	33.2

**Table 7.** Comparison of NAC and R<sub>NO2</sub> before and after sulfurization of LS0 and LS5 catalysts.

Catalyst	NAC (μmol/g)		R <sub>NO2</sub>		The Decline Rate of NAC
	Fresh	Sulfur Poisoning	Fresh	Sulfur Poisoning	
LS0	831	554	52	19	33.3
LS5	1889	1434	63	28	24.2

Overall, the LS5 catalyst exhibits a wide operating temperature range (200–400 °C), with higher NAC (750–1899 μmol/g) and NSC (80–1084 μmol/g), which indicates its excellent ability to capture NO<sub>x</sub> at low to medium temperatures. In addition, the LS5 catalyst also exhibits excellent stability after hydrothermal and sulfur poisoning. Consequently, LS5 can be considered a promising material for NO<sub>x</sub> storage.

### 3.9. IR Study of NO<sub>x</sub> Storage

In order to determine the storage species of the samples, FTIR analysis was conducted on the catalysts after NO<sub>x</sub> storage. The results, depicted in Figure 10, reveal that the predominant adsorbed species on the LSX surface are primarily bulk nitrate (736 cm<sup>-1</sup>, 814 cm<sup>-1</sup>), nitrate ions (1360 cm<sup>-1</sup>, 1384 cm<sup>-1</sup>) [53], and bidentate nitrate (1502 cm<sup>-1</sup>) (1502 cm<sup>-1</sup>) [54,55]. Additionally, the characteristic peak at 580 cm<sup>-1</sup> corresponds to the perovskite structure, while peaks at 667, 858, and 1451 cm<sup>-1</sup> indicate the presence of carbonate species. Lastly, the peak at 1633 cm<sup>-1</sup> is attributed to H<sub>2</sub>O. Overall, the NO<sub>x</sub>

storage on LS0 and LS5 catalysts follows the “nitrate” route, aligning with the findings of the  $\text{NO}_x$  desorption stage (Figures 8 and 9).

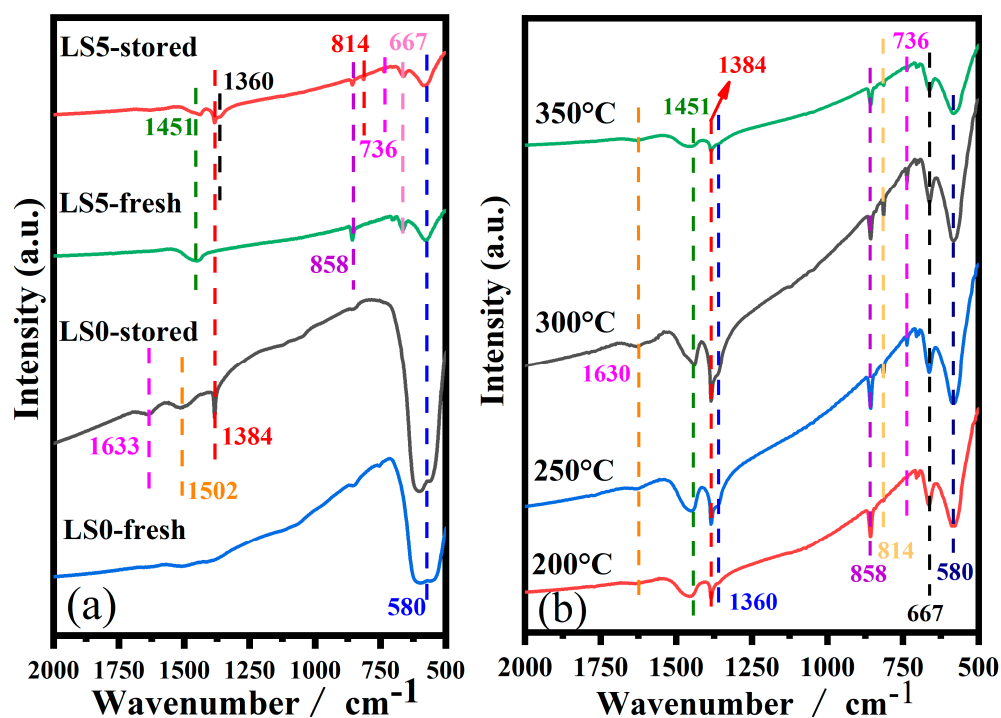


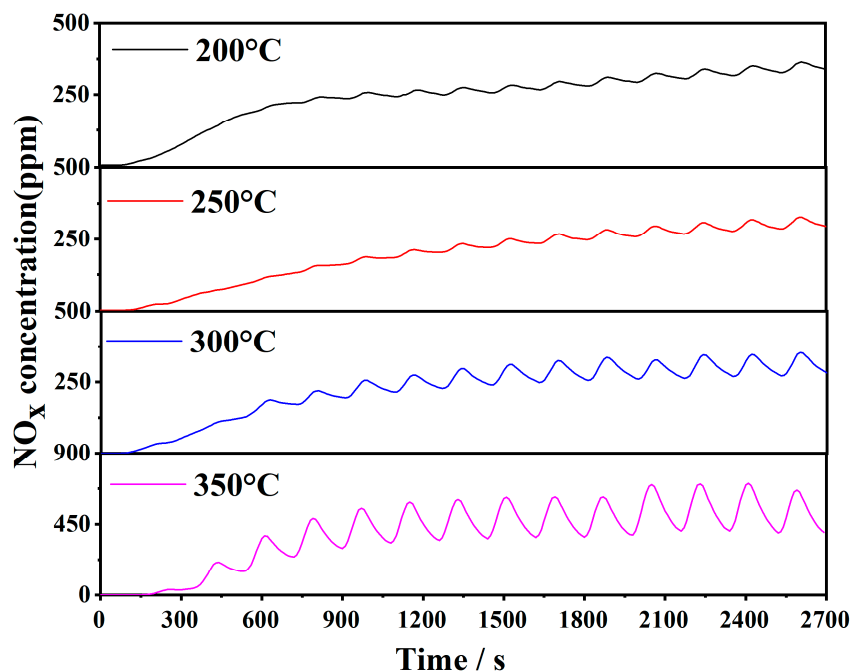
**Figure 10.** (a) IR spectra of the LSX catalysts before and after  $\text{NO}_x$  storage at 300 °C; (b) IR spectra of LS5 at different  $\text{NO}_x$  storage temperatures.

As illustrated in Figure 10a, the LS0 catalyst exhibits nitrate ions and bidentate nitrate species as the stored  $\text{NO}_x$ , with the storage phase consisting solely of the perovskite phase. On the other hand, the LS5 catalyst displays stored  $\text{NO}_x$  in the form of nitrate ions and bulk nitrate species. Notably, the peak of carbonate diminishes while, the peak of bulk nitrate species emerges after storage, suggesting a possible conversion from carbonate to bulk nitrate. Moreover, the storage phase consists of perovskite and strontium carbonate following Sr doping [56]. Consequently, it can be inferred that the LS5 catalyst demonstrates favorable NAC and NSC, with the presence of  $\text{SrCO}_3$  contributing to this effect.

Based on Figure 10b, LS5 adsorbs  $\text{NO}_x$  at different storage temperatures and stores it as bulk nitrates and nitrate ions, indicating that the storage phase encompasses both perovskite and strontium carbonate. The intensity of the nitrate species peaks increases as the temperature rises from 200 °C to 300 °C. However, beyond 350 °C, the intensity diminishes, suggesting a decline in the storage phase’s effectiveness at this temperature. Notably, the catalyst exhibits the strongest infrared peak of nitrate at 300 °C, aligning with the LS5’s maximum adsorption–desorption capacity at this temperature.

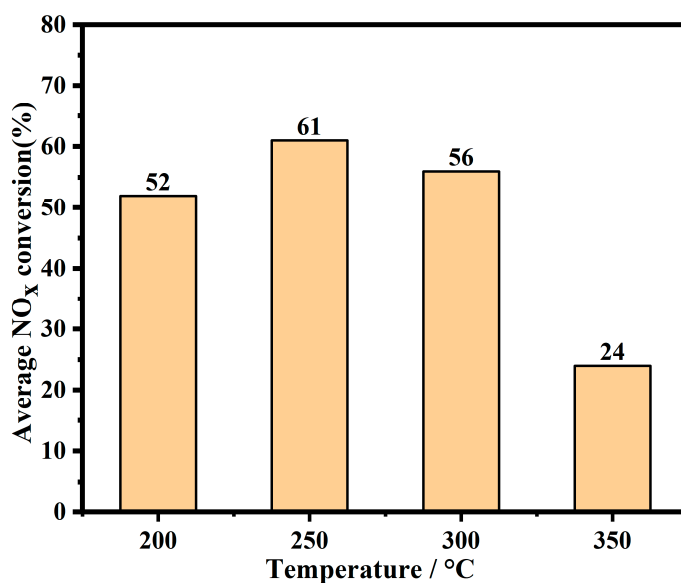
### 3.10. $\text{NO}_x$ Storage and Reduction Performance

Figure 11 displays the results of lean–rich cycling tests performed on the LS5 sample at different temperatures. During the lean periods,  $\text{NO}$  undergoes oxidation to  $\text{NO}_2$  and is subsequently stored as nitrates. In the rich periods, the stored nitrates decompose and release  $\text{NO}_x$  [31]. The released  $\text{NO}_x$  is reduced by  $\text{C}_3\text{H}_8$ . At different reaction temperatures, there is minimal release of  $\text{NO}_x$  in the first cycle, indicating complete reduction of  $\text{NO}_x$  by  $\text{C}_3\text{H}_8$ . However, as the number of cycles increases, the concentration of  $\text{NO}_x$  gradually rises while the conversion of  $\text{NO}_x$  decreases. This can be attributed to the stable storage of  $\text{NO}_x$ , which occupies the storage sites, and the partial deactivation of active sites on the catalysts, resulting in lower reduction efficiency.



**Figure 11.** NO<sub>x</sub> concentration curves of the LS5 catalyst during the NSR process at different temperatures (200–350 °C).

Figure 12 displays the average NO<sub>x</sub> conversion of the LS5 catalyst at different temperatures. As shown, the catalyst achieves an average NO<sub>x</sub> removal rate of over 52% within the temperature range of 200–300 °C, with maximum NO<sub>x</sub> removal of 61% observed at 250 °C. Subsequently, as the reaction temperature increases, the average NO<sub>x</sub> conversion decreases. These findings align with the adsorption and desorption behavior of NO<sub>x</sub>. It is likely that the positive correlation between temperature and nitrate stability hampers the decomposition of nitrate and catalyst regeneration, thereby reducing the average NO<sub>x</sub> removal rate. In conclusion, when utilizing C<sub>3</sub>H<sub>8</sub> as the reducing gas, the LS5 catalyst exhibits a superior average NO<sub>x</sub> conversion rate at low temperatures.



**Figure 12.** Average NO<sub>x</sub> conversion of the LS5 catalyst at different temperatures during lean-rich cycling experiments.

#### 4. Conclusions

In summary, the perovskite  $\text{La}_{1-x}\text{Sr}_x\text{Co}_{1-\lambda}\text{O}_{3-\delta}$  nanomaterials were successfully synthesized using the solution combustion method. The incorporation of Sr strongly influences the crystalline phase, textural properties, desorption of surface oxygen species, and redox performance of the perovskite catalysts. As a result, it promotes the NO oxidation,  $\text{NO}_x$  adsorption and storage, and  $\text{NO}_x$  reduction. In addition, the incorporation of Sr enables the catalysts to exhibit superior resistance to hydrothermal aging and sulfur. The adsorption of  $\text{NO}_x$  over LSX catalysts at 300 °C occurs predominantly via the “nitrate route”. Substituting 50% of  $\text{La}^{3+}$  with  $\text{Sr}^{2+}$  doubled the  $\text{NO}_x$  adsorption capacity of perovskite  $\text{LaCoO}_3$  at 300 °C, which could be attributed to the large surface area, strong reducibility, more surface oxygen species, and elevated surface  $\text{Co}^{2+}$  concentration. During the lean-rich cycling experiments, the LS5 catalyst achieved an average  $\text{NO}_x$  conversion rate of over 50% in the temperature range of 200–300 °C, with a maximum  $\text{NO}_x$  conversion of 61% recorded at 250 °C. Thus, Sr-doped  $\text{LaCoO}_3$  perovskite catalysts prepared using the solution combustion method demonstrate outstanding  $\text{NO}_x$  storage performance at low–medium temperatures, making them a potential material for De- $\text{NO}_x$  applications.

**Author Contributions:** Conceptualization: Z.W. and L.G.; Methodology: Z.W., W.L. and L.W.; Formal analysis and investigation: X.L., X.W., T.Z., J.L. and Y.Z.; Writing—original draft: X.L.; Writing—review and editing: Z.W.; Funding acquisition: Z.W.; Resources: Z.W.; Supervision: Z.W. All authors have read and agreed to the published version of the manuscript.

**Funding:** This work was financially supported by the Natural Science Foundation of Shandong Province (Nos. ZR2023MB100, ZR2021MB063, ZR2020MB120), National Natural Science Foundation of China (No. 21777055), and Innovation ability improvement project of technology-based small and medium-sized enterprises in Shandong Province (Nos. 2022TSGC2043, 2021TSGC1358).

**Institutional Review Board Statement:** Not applicable.

**Data Availability Statement:** The data presented in this study are available on request from the corresponding author.

**Conflicts of Interest:** The authors declare no conflicts of interest.

#### References

1. Epling, W.S.; Parks, J.E.; Campbell, G.C.; Yezerets, A.; Currier, N.W.; Campbell, L.E. Further evidence of multiple  $\text{NO}_x$  sorption sites on  $\text{NO}_x$  storage/reduction catalysts. *Catal. Today* **2004**, *96*, 21–30. [[CrossRef](#)]
2. Pereda-Ayo, B.; De La Torre, U.; Illán-Gómez, M.J.; Bueno-López, A.; González-Velasco, J.R. Role of the different copper species on the activity of Cu/zeolite catalysts for SCR of  $\text{NO}_x$  with  $\text{NH}_3$ . *Appl. Catal. B Environ.* **2014**, *147*, 420–428. [[CrossRef](#)]
3. Salasc, S.; Skoglundh, M.; Fridell, E. A comparison between Pt and Pd in  $\text{NO}_x$  storage catalysts. *Appl. Catal. B Environ.* **2002**, *36*, 145–160. [[CrossRef](#)]
4. Castoldi, L.; Matarrese, R.; Morandi, S.; Righini, L.; Lietti, L. New insights on the adsorption, thermal decomposition and reduction of  $\text{NO}_x$  over Pt- and Ba-based catalysts. *Appl. Catal. B Environ.* **2018**, *224*, 249–263. [[CrossRef](#)]
5. Ecker, S.I.; Dornseiffer, J.; Werner, J.; Schlenz, H.; Sohn, Y.J.; Sauerwein, F.S.; Baumann, S.; Bouwmeester, H.J.M.; Guillon, O.; Weirich, T.E.; et al. Novel low-temperature lean  $\text{NO}_x$  storage materials based on  $\text{La}_{0.5}\text{Sr}_{0.5}\text{Fe}_{1-x}\text{M}_x\text{O}_{3-\delta}/\text{Al}_2\text{O}_3$  infiltration composites (M = Ti, Zr, Nb). *Appl. Catal. B Environ.* **2021**, *286*, 119919. [[CrossRef](#)]
6. You, R.; Zhang, Y.; Liu, D.; Meng, M.; Jiang, Z.; Zhang, S.; Huang, Y. A series of ceria supported lean-burn  $\text{NO}_x$  trap catalysts  $\text{LaCoO}_3/\text{K}_2\text{CO}_3/\text{CeO}_2$  using perovskite as active component. *Chem. Eng. J.* **2015**, *260*, 357–367. [[CrossRef](#)]
7. Onrubia-Calvo, J.A.; Pereda-Ayo, B.; De-La-Torre, U.; Gonzalez-Velasco, J.R. Strontium doping and impregnation onto alumina improve the  $\text{NO}_x$  storage and reduction capacity of  $\text{LaCoO}_3$  perovskites. *Catal. Today* **2019**, *333*, 208–218. [[CrossRef](#)]
8. Pereda-Ayo, B.; De La Torre, U.; Pilar Gonzalez-Marcos, M.; Gonzalez-Velasco, J.R. Influence of ceria loading on the  $\text{NO}_x$  storage and reduction performance of model Pt-Ba/ $\text{Al}_2\text{O}_3$  NSR catalyst. *Catal. Today* **2015**, *241*, 133–142. [[CrossRef](#)]
9. Mráček, D.; Kočí, P.; Choi, J.-S.; Partridge, W.P. New operation strategy for driving the selectivity of  $\text{NO}_x$  reduction to  $\text{N}_2$ ,  $\text{NH}_3$  or  $\text{N}_2\text{O}$  during lean/rich cycling of a lean  $\text{NO}_x$  trap catalyst. *Appl. Catal. B Environ.* **2016**, *182*, 109–114. [[CrossRef](#)]
10. Fernandes, D.M.; Scofield, C.F.; Neto, A.A.; Cardoso, M.J.B.; Zotin, F.M.Z. Thermal deactivation of Pt/Rh commercial automotive catalysts. *Chem. Eng. J.* **2010**, *160*, 85–92. [[CrossRef](#)]
11. Peng, Y.; Si, W.; Luo, J.; Su, W.; Chang, H.; Li, J.; Hao, J.; Crittenden, J. Surface Tuning of  $\text{La}_{0.5}\text{Sr}_{0.5}\text{CoO}_3$  Perovskite Catalysts by Acetic Acid for  $\text{NO}_x$  Storage and Reduction. *Environ. Sci. Technol.* **2016**, *50*, 6442–6448. [[CrossRef](#)]

12. Uran, L.; Gallego, J.; Li, W.Y.; Santamaria, A. Effect of catalyst preparation for the simultaneous removal of soot and NO<sub>x</sub>. *Appl. Catal. A Gen.* **2019**, *569*, 157–169. [[CrossRef](#)]
13. Ueda, A.; Yamada, Y.; Katsuki, M.; Kiyobayashi, T.; Xu, Q.; Kuriyama, N. Perovskite catalyst (La, Ba)(Fe, Nb, Pd)O<sub>3</sub> applicable to NO<sub>x</sub> storage and reduction system. *Catal. Commun.* **2009**, *11*, 34–37. [[CrossRef](#)]
14. Panunzi, A.P.; Duranti, L.; Luisetto, I.; Lisi, N.; Marelli, M.; Di Bartolomeo, E. Triggering electrode multi-catalytic activity for reversible symmetric solid oxide cells by Pt-doping lanthanum strontium ferrite. *Chem. Eng. J.* **2023**, *471*, 144448. [[CrossRef](#)]
15. Ji, K.; Dai, H.; Deng, J.; Jiang, H.; Zhang, L.; Zhang, H.; Cao, Y. Catalytic removal of toluene over three-dimensionally ordered macroporous Eu<sub>1-x</sub>Sr<sub>x</sub>FeO<sub>3</sub>. *Chem. Eng. J.* **2013**, *214*, 262–271. [[CrossRef](#)]
16. Onrubia-Calvo, J.A.; Pereda-Ayo, B.; De-La-Torre, U.; González-Velasco, J.R. Key factors in Sr-doped LaBO<sub>3</sub> (B = Co or Mn) perovskites for NO oxidation in efficient diesel exhaust purification. *Appl. Catal. B Environ.* **2017**, *213*, 198–210. [[CrossRef](#)]
17. Kim, C.H.; Qi, G.; Dahlberg, K.; Li, W. Strontium-doped perovskites rival platinum catalysts for treating NO<sub>x</sub> in simulated diesel exhaust. *Science* **2010**, *327*, 1624–1627. [[CrossRef](#)]
18. Say, Z.; Mihai, O.; Kurt, M.; Olsson, L.; Ozensoy, E. Trade-off between NO<sub>x</sub> storage capacity and sulfur tolerance on Al<sub>2</sub>O<sub>3</sub>/ZrO<sub>2</sub>/TiO<sub>2</sub>-based DeNO<sub>x</sub> catalysts. *Catal. Today* **2019**, *320*, 152–164. [[CrossRef](#)]
19. Say, Z.; Vovk, E.I.; Bukhtiyarov, V.I.; Ozensoy, E. Enhanced Sulfur Tolerance of Ceria-Promoted NO<sub>x</sub> Storage Reduction (NSR) Catalysts: Sulfur Uptake, Thermal Regeneration and Reduction with H<sub>2</sub>(g). *Top. Catal.* **2013**, *56*, 950–957. [[CrossRef](#)]
20. Theis, J.R. An assessment of Pt and Pd model catalysts for low temperature NO<sub>x</sub> adsorption. *Catal. Today* **2016**, *267*, 93–109. [[CrossRef](#)]
21. Elbouazzaoui, S.; Corbos, E.C.; Courtois, X.; Marecot, P.; Duprez, D. A study of the deactivation by sulfur and regeneration of a model NSR Pt/Ba/Al<sub>2</sub>O<sub>3</sub> catalyst. *Appl. Catal. B Environ.* **2005**, *61*, 236–243. [[CrossRef](#)]
22. Varma, A.; Mukasyan, A.S.; Rogachev, A.S.; Manukyan, K.V. Solution Combustion Synthesis of Nanoscale Materials. *Chem. Rev.* **2016**, *116*, 14493–14586. [[CrossRef](#)]
23. Park, J.-H.; Cho, H.J.; Park, S.J.; Nam, I.-S.; Yeo, G.K.; Kil, J.K.; Youn, Y.K. Role of cobalt on γ-Al<sub>2</sub>O<sub>3</sub> based NO<sub>x</sub> storage catalyst. *Top. Catal.* **2007**, *42*, 61–64. [[CrossRef](#)]
24. Ao, M.; Pham, G.H.; Sage, V.; Pareek, V. Structure and activity of strontium substituted LaCoO<sub>3</sub> perovskite catalysts for syngas conversion. *J. Mol. Catal. A Chem.* **2016**, *416*, 96–104. [[CrossRef](#)]
25. Hueso, J.L.; Holgado, J.P.; Pereñíguez, R.; Mun, S.; Salmeron, M.; Caballero, A. Chemical and electronic characterization of cobalt in a lanthanum perovskite. Effects of strontium substitution. *J. Solid State Chem.* **2010**, *183*, 27–32. [[CrossRef](#)]
26. Villoria, J.A.; Alvarez-Galvan, M.C.; Al-Zahrani, S.M.; Palmisano, P.; Specchia, S.; Specchia, V.; Fierro, J.L.G.; Navarro, R.M. Oxidative reforming of diesel fuel over LaCoO<sub>3</sub> perovskite derived catalysts: Influence of perovskite synthesis method on catalyst properties and performance. *Appl. Catal. B Environ.* **2011**, *105*, 276–288. [[CrossRef](#)]
27. Specchia, S.; Galletti, C.; Specchia, V. Solution Combustion Synthesis as intriguing technique to quickly produce performing catalysts for specific applications. In *Studies in Surface Science and Catalysis*; Gaigneaux, E.M., Devillers, M., Hermans, S., Jacobs, P.A., Martens, J.A., Ruiz, P., Eds.; Elsevier: Amsterdam, The Netherlands, 2010; pp. 59–67.
28. Feng, N.; Meng, J.; Wu, Y.; Chen, C.; Wang, L.; Gao, L.; Wan, H.; Guan, G. KNO<sub>3</sub> supported on three-dimensionally ordered macroporous La<sub>0.8</sub>Ce<sub>0.2</sub>Mn<sub>1-x</sub>Fe<sub>x</sub>O<sub>3</sub> for soot removal. *Catal. Sci. Technol.* **2016**, *6*, 2930–2941. [[CrossRef](#)]
29. Groen, J.C.; Peffer, L.A.A.; Pérez-Ramírez, J. Pore size determination in modified micro- and mesoporous materials. Pitfalls and limitations in gas adsorption data analysis. *Microporous Mesoporous Mater.* **2003**, *60*, 1–17. [[CrossRef](#)]
30. Wang, Y.; Zhu, Y.; Liu, S.; Zhang, R. Pore characterization and its impact on methane adsorption capacity for organic-rich marine shales. *Fuel* **2016**, *181*, 227–237. [[CrossRef](#)]
31. Cui, C.; Ma, J.; Wang, Z.; Liu, W.; Liu, W.; Wang, L. High Performance of Mn-Doped MgAlO<sub>x</sub> Mixed Oxides for Low Temperature NO<sub>x</sub> Storage and Release. *Catalysts* **2019**, *9*, 677. [[CrossRef](#)]
32. Liang, H.; Mou, Y.; Zhang, H.; Li, S.; Yao, C.; Yu, X. Sulfur resistance and soot combustion for La<sub>0.8</sub>K<sub>0.2</sub>Co<sub>1-y</sub>Mn<sub>y</sub>O<sub>3</sub> catalyst. *Catal. Today* **2017**, *281*, 477–481. [[CrossRef](#)]
33. Montanari, T.; Castoldi, L.; Lietti, L.; Busca, G. Basic catalysis and catalysis assisted by basicity: FT-IR and TPD characterization of potassium-doped alumina. *Appl. Catal. A Gen.* **2011**, *400*, 61–69. [[CrossRef](#)]
34. Li, Q.; Wang, X.; Xin, Y.; Zhang, Z.; Zhang, Y.; Hao, C.; Meng, M.; Zheng, L.; Zheng, L. A unified intermediate and mechanism for soot combustion on potassium-supported oxides. *Sci. Rep.* **2014**, *4*, 4725. [[CrossRef](#)] [[PubMed](#)]
35. Morales, M.; Segarra, M. Steam reforming and oxidative steam reforming of ethanol over La<sub>0.6</sub>Sr<sub>0.4</sub>CoO<sub>3</sub>-delta perovskite as catalyst precursor for hydrogen production. *Appl. Catal. A Gen.* **2015**, *502*, 305–311. [[CrossRef](#)]
36. Li, Z.; Meng, M.; Zha, Y.; Dai, F.; Hu, T.; Xie, Y.; Zhang, J. Highly efficient multifunctional dually-substituted perovskite catalysts La<sub>1-x</sub>K<sub>x</sub>Co<sub>1-y</sub>Cu<sub>y</sub>O<sub>3-δ</sub> used for soot combustion, NO<sub>x</sub> storage and simultaneous NO<sub>x</sub>-soot removal. *Appl. Catal. B Environ.* **2012**, *121–122*, 65–74. [[CrossRef](#)]
37. Stangeland, K.; Kalai, D.Y.; Ding, Y.; Yu, Z.X. Mesoporous manganese-cobalt oxide spinel catalysts for CO<sub>2</sub> hydrogenation to methanol. *J. CO<sub>2</sub> Util.* **2019**, *32*, 146–154. [[CrossRef](#)]
38. Wang, X.; Zuo, J.; Luo, Y.; Jiang, L. New route to CeO<sub>2</sub>/LaCoO<sub>3</sub> with high oxygen mobility for total benzene oxidation. *Appl. Surf. Sci.* **2017**, *396*, 95–101. [[CrossRef](#)]

39. Crumlin, E.J.; Mutoro, E.; Liu, Z.; Grass, M.E.; Biegalski, M.D.; Lee, Y.-L.; Morgan, D.; Christen, H.M.; Bluhm, H.; Shao-Horn, Y. Surface strontium enrichment on highly active perovskites for oxygen electrocatalysis in solid oxide fuel cells. *Energy Environ. Sci.* **2012**, *5*, 6081–6088. [[CrossRef](#)]
40. Bai, B.; Arandiyani, H.; Li, J. Comparison of the performance for oxidation of formaldehyde on nano-Co<sub>3</sub>O<sub>4</sub>, 2D-Co<sub>3</sub>O<sub>4</sub>, and 3D-Co<sub>3</sub>O<sub>4</sub> catalysts. *Appl. Catal. B Environ.* **2013**, *142*, 677–683. [[CrossRef](#)]
41. Zhang, B.; Yu, C.; Li, Z. Enhancing the Electrochemical Properties of LaCoO<sub>3</sub> by Sr-Doping, rGO-Compounding with Rational Design for Energy Storage Device. *Nanoscale Res. Lett.* **2020**, *15*, 184. [[CrossRef](#)]
42. Arandiyani, H.; Dai, H.; Deng, J.; Liu, Y.; Bai, B.; Wang, Y.; Li, X.; Xie, S.; Li, J. Three-dimensionally ordered macroporous La<sub>0.6</sub>Sr<sub>0.4</sub>MnO<sub>3</sub> with high surface areas: Active catalysts for the combustion of methane. *J. Catal.* **2013**, *307*, 327–339. [[CrossRef](#)]
43. Akay, G. Plasma Generating-Chemical Looping Catalyst Synthesis by Microwave Plasma Shock for Nitrogen Fixation from Air and Hydrogen Production from Water for Agriculture and Energy Technologies in Global Warming Prevention. *Catalysts* **2020**, *10*, 152. [[CrossRef](#)]
44. Akay, G. Hydrogen, Ammonia and Symbiotic/Smart Fertilizer Production Using Renewable Feedstock and CO<sub>2</sub> Utilization through Catalytic Processes and Nonthermal Plasma with Novel Catalysts and In Situ Reactive Separation: A Roadmap for Sustainable and Innovation-Based Technology. *Catalysts* **2023**, *13*, 1287. [[CrossRef](#)]
45. Zakaryan, H.A.; Aroutiounian, V.M. Investigation of cobalt doped tin dioxide structure and defects: Density functional theory and empirical force fields. *J. Contemp. Phys. Armen. Acad. Sci.* **2017**, *52*, 227–233. [[CrossRef](#)]
46. Catto, A.C.; da Silva, L.F.; Bernardi, M.I.B.; Bernardini, S.; Aguir, K.; Longo, E.; Mastelaro, V.R. Local Structure and Surface Properties of Co<sub>x</sub>Zn<sub>1-x</sub>O Thin Films for Ozone Gas Sensing. *ACS Appl. Mater. Interfaces* **2016**, *8*, 26066–26072. [[CrossRef](#)] [[PubMed](#)]
47. Zhang, Y.; Yu, Y.; Shan, W.; Lian, Z.; He, H. Effect of support preparation with different concentration precipitant on the NO<sub>x</sub> storage performance of Pt/BaO/CeO<sub>2</sub> catalysts. *Catal. Today* **2020**, *339*, 135–147. [[CrossRef](#)]
48. Liu, W.; Cao, H.; Wang, Z.; Cui, C.; Gan, L.; Liu, W.; Wang, L. A novel ceria hollow nanosphere catalyst for low temperature NO<sub>x</sub> storage. *J. Rare Earths* **2022**, *40*, 626–635. [[CrossRef](#)]
49. Fridell, E.; Persson, H.; Westerberg, B.; Olsson, L.; Skoglundh, M. The mechanism for NO<sub>x</sub> storage. *Catal. Lett.* **2000**, *66*, 71–74. [[CrossRef](#)]
50. Wang, X.Y.; Qi, X.X.; Chen, Z.L.; Jiang, L.L.; Wang, R.H.; Wei, K.M. Studies on SO<sub>2</sub> Tolerance and Regeneration over Perovskite-Type LaCo<sub>1-x</sub>Pt<sub>x</sub>O<sub>3</sub> in NO<sub>x</sub> Storage and Reduction. *J. Phys. Chem. C* **2014**, *118*, 13743–13751. [[CrossRef](#)]
51. Wen, W.; Wang, X.Y.; Jin, S.; Wang, R.H. LaCoO<sub>3</sub> perovskite in Pt/LaCoO<sub>3</sub>/K/Al<sub>2</sub>O<sub>3</sub> for the improvement of NO<sub>x</sub> storage and reduction performances. *RSC Adv.* **2016**, *6*, 74046–74052. [[CrossRef](#)]
52. Xie, W.; Xu, G.; Zhang, Y.; Yu, Y.; He, H. Mesoporous LaCoO<sub>3</sub> perovskite oxide with high catalytic performance for NO<sub>x</sub> storage and reduction. *J. Hazard. Mater.* **2022**, *431*, 128528. [[CrossRef](#)]
53. Xian, H.; Zhang, X.; Li, X.; Li, L.; Zou, H.; Meng, M.; Li, Q.; Tan, Y.; Tsubaki, N. BaFeO<sub>3-x</sub> Perovskite: An Efficient NO<sub>x</sub> Absorber with a High Sulfur Tolerance. *J. Phys. Chem. C* **2010**, *114*, 11844–11852. [[CrossRef](#)]
54. You, R.; Zhang, Y.; Liu, D.; Meng, M.; Zheng, L.; Zhang, J.; Hu, T. YCeZrO Ternary Oxide Solid Solution Supported Nonplatinic Lean-Burn NO<sub>x</sub> Trap Catalysts Using LaCoO<sub>3</sub> Perovskite as Active Phase. *J. Phys. Chem. C* **2014**, *118*, 25403–25420. [[CrossRef](#)]
55. Hadjiivanov, K. Identification of neutral and charged N<sub>x</sub>O<sub>y</sub> surface species by IR spectroscopy. *Catal. Rev. Sci. Eng.* **2000**, *42*, 144–171. [[CrossRef](#)]
56. Li, X.-G.; Dong, Y.-H.; Xian, H.; Hernandez, W.Y.; Meng, M.; Zou, H.-H.; Ma, A.-J.; Zhang, T.-Y.; Jiang, Z.; Tsubaki, N.; et al. De-NO<sub>x</sub> in alternative lean/rich atmospheres on La<sub>1-x</sub>Sr<sub>x</sub>CoO<sub>3</sub> perovskites. *Energy Environ. Sci.* **2011**, *4*, 3351–3354. [[CrossRef](#)]

**Disclaimer/Publisher's Note:** The statements, opinions and data contained in all publications are solely those of the individual author(s) and contributor(s) and not of MDPI and/or the editor(s). MDPI and/or the editor(s) disclaim responsibility for any injury to people or property resulting from any ideas, methods, instructions or products referred to in the content.